

UAV's Rotor Micro-Doppler Feature Extraction Using Integrated Sensing and Communication Signal: Algorithm Design and Testbed Evaluation

Jiachen Wei, Dingyou Ma, Feiyang He, Qixun Zhang, Zhiyong Feng, Zhengfeng Liu, Taohong Liang

Abstract—With the rapid application of unmanned aerial vehicles (UAVs) in urban areas, the identification and tracking of hovering UAVs have become critical challenges, significantly impacting the safety of aircraft take-off and landing operations. As a promising technology for 6G mobile systems, integrated sensing and communication (ISAC) can be used to detect high-mobility UAVs with a low deployment cost. The micro-Doppler signals from UAV rotors can be leveraged to address the detection of low-mobility and hovering UAVs using ISAC signals. However, determining whether the frame structure of the ISAC system can be used to identify UAVs, and how to accurately capture the weak rotor micro-Doppler signals of UAVs in complex environments, remain two challenging problems. This paper first proposes a novel frame structure for UAV micro-Doppler extraction and the representation of UAV micro-Doppler signals within the channel state information (CSI). Furthermore, to address complex environments and the interference caused by UAV body vibrations, the rotor micro-Doppler null space pursuit (rmD-NSP) algorithm and the feature extraction algorithm synchroextracting transform (SET) are designed to effectively separate UAV's rotor micro-Doppler signals and enhance their features in the spectrogram. Finally, both simulation and hardware testbed demonstrate that the proposed rmD-NSP algorithm enables the ISAC base station (BS) to accurately and completely extract UAV's rotor micro-Doppler signals. Within a 0.1 s observation period, ISAC BS successfully captures eight rotations of the DJI M300 RTK UAV's rotor in urban environments. Compared to the existing AM-FM NSP and NSP signal decomposition algorithms, the integrity of the rotor micro-Doppler features is improved by 60%.

Index Terms—Integrated sensing and communication, UAV micro-Doppler, Null space pursuit, Feature extraction.

I. INTRODUCTION

The rapid development of 5G mobile communication systems and artificial intelligence technology has drawn significant attention to the low-altitude economy [1]. The low cost, small size, ease of acquisition, and particularly live video feed have greatly popularized the use of unmanned aerial vehicles (UAVs). Unfortunately, the increasing popularity of UAV applications has raised concerns about safety, security,

and privacy, mainly due to the so-called smart attacks and threats [2]. It is critically important to find ways to counter the illegal UAVs intrusion [3]. Therefore, numerous researchers from academia and industry have tried to develop suitable UAV detection systems, primarily through the use of multiple sensors, such as ultrasonic sensors, light detection and ranging (LiDAR), optical cameras, millimeter wave (mmWave) radars, etc. At the same time, the next generation of wireless networks, in addition to providing primary communication functions, is also expected to gain the capability to sense the surrounding environment through radio frequency (RF) signals, effectively acting as a sensor [4]. Leveraging existing communication base stations (BSs) and pipeline infrastructure, a UAV detection network can be rapidly and cost-effectively constructed. Furthermore, the inherent network collaborative capability of multiple BSs can enhance the detection accuracy and reduce blind spot detection, which can address the problem of UAV being difficult to detect in urban scenarios [5].

As one of the key technologies for 6G communication, integrated sensing and communication (ISAC) systems provide theoretical feasibility for using mobile communication systems to detect UAVs [6]. Current research on ISAC primarily focuses on four aspects: signal design [7]–[9], signal processing [10]–[12], protocol-based applications [13]–[16], and networking sensing [17]–[19]. In scenarios where multiple BSs are used to detect UAVs, current research mainly focuses on UAV localization and tracking [20]–[22]. Specifically, these ISAC signal processing algorithms assume that the UAV is a point target with strong reflections and high-speed movement characteristics. These assumptions cannot align with the actual situations [23]–[26]. First, the assumption that the UAV is a single scatterer neglects the reflections from the rotor blades. Second, UAV typically move at a slower speed and can hover, making them difficult to detect from clutter, noise, and other natural flying objects like birds in urban environments. Actually, the rotation of the UAV's rotor introduces unique high-frequency modulation sidebands near the Doppler frequency, known as the micro-Doppler signal. This micro-Doppler signal can be used to identify the type of target and distinguish it from other objects [27].

However, existing ISAC studies do not consider the application of micro-Doppler to detect and identify UAV in mobile communication systems. There is still a lack of practical performance evaluation for using mobile communication systems to extract micro-Doppler signatures of UAV. The challenges with micro-Doppler extraction of UAV based on mobile com-

This work is partly supported by Beijing Natural Science Foundation (L232003), National Natural Science Foundation of China (62321001, 62341101), Fundamental Research Funds for the Central Universities (No. 24820232023YQTD01) and Fundamental Research Funds for the Central Universities (2024RC02).

J. Wei, D. Ma, F. He, Q. Zhang, Z. Feng, Z. Liu, and T. Liang are with the Key Laboratory of Universal Wireless Communications, Ministry of Education, Beijing University of Posts and Telecommunications, Beijing 100876, China (Email: {weijiachen, dingyouma}@bupt.edu.cn, flyinghjgc@163.com, {zhangqixun, fengzy}@bupt.edu.cn, guan_kangping@163.com, 13381221925@189.cn).

(Corresponding authors: Dingyou Ma)

munication systems come from two main sources. One aspect is whether the communication waveform and uplink/downlink frame structure affect the micro-Doppler feature extraction of UAVs. On the other hand, considering the complex environment faced by micro-Doppler signal extraction, there is a significant amount of clutter and interference. The UAV's rotor echoes to be extracted are very weak, making the extraction of micro-Doppler features challenging. Furthermore, the vibration of UAVs itself also affects the performance of micro-Doppler extraction [28], [29].

Therefore, to address the above issues, this paper presents a time division duplexing (TDD) frame structure configuration for extracting micro-Doppler features of UAV using ISAC signal. Furthermore, it provides an expression for the echoes of UAV in the context of channel state information (CSI). This expression takes into account the time-varying radar cross section (RCS) caused by the UAV's rotor rotation, leading to periodic variations in rotor echo intensity. Additionally, it considers the translational and vibrational motion models of the UAV body. To combat the complex environment and suppress the effect of body vibrations, the rotor micro-Doppler null space pursuit (rmD-NSP) algorithm is designed, based on an operator-based signal decomposition method [30]–[32], to extract weak rotor micro-Doppler signals from various interference signals. The rotor micro-Doppler signals obtained from decomposition can be further processed using the synchroextracting transform (SET) algorithm to obtain time-frequency ridges with more concentrated energy, thus revealing more pronounced micro-Doppler features [33]. Finally, both simulation and hardware testbed results demonstrate that the proposed rmD-NSP algorithm can extract more UAV rotor micro-Doppler signals in urban environments compared to existing AM-FM NSP [32] and NSP [30] signal decomposition algorithms. The main contributions of this paper are summarized as follows.

- A new mathematical model for micro-Doppler of UAV in monostatic ISAC systems is proposed. This paper provides a model for the representation of the micro-Doppler signal in the CSI and considers the rotation of multiple rotor blades of UAVs, as well as the translational motion and vibration of the UAV body during flight. Additionally, the mathematical model takes into account the dynamic RCS of rotors caused by the rotation of the blade, which will be an interesting tool for the future development of ISAC target classification algorithms.
- We design a rmD-NSP adaptive operator based on the mathematical model of the UAV rotor. Through the zero space tracking algorithm, we extract rotor micro-Doppler signals from mixed signal containing many interference components. In addition, we use the time-frequency enhancement algorithm SET to complete the extraction of the micro-Doppler feature of UAVs.
- By conducting software simulations and hardware testbed based on the ISAC system, we validated the effectiveness of using the rmD-NSP algorithm and SET algorithm to extract the micro-Doppler feature of UAVs in mobile communication systems. Within a 0.1 s observation pe-

riod, ISAC BS successfully captures eight rotations of the DJI M300 RTK UAV's rotor in urban environment.

The rest of this paper is organized as follows. Section II presents the system model of the UAV micro-Doppler feature extraction. Section III introduces the rmD-NSP algorithm and the SET algorithm. In Section IV, we present the software simulation results. In Section V, we implement the extraction of micro-Doppler features from UAVs using the ISAC hardware testbed. Section VI concludes this paper.

The following notations are used throughout this paper: Boldface lowercase and uppercase letters denote vectors and matrices, respectively. We denote the transpose operation as $(\cdot)^T$. $\mathbf{A}_x = \text{diag}(\mathbf{x})$ denotes the diagonalization of the vector \mathbf{x} . The set of complex numbers is \mathbb{C} and the set of real numbers is \mathbb{R} .

II. SYSTEM MODEL

In this section, we consider an ISAC BS to implement the micro-Doppler feature extraction function for UAV, as shown in Fig. 1 (a). The BS is equipped with separate antennas that enable full-duplex functionality, enabling it to transmit and receive signals simultaneously.

First, in Subsection II-A, we present a frame structure based on 3GPP TS 38.211 [34] for extracting UAV micro-Doppler features using BS, as shown in Fig. 1 (b). In Subsection II-B, we present the ISAC echo representation of the UAV, considering the dynamic RCS characteristics and rotational motion of rotors, as well as the translational and vibrational motion of the UAV body. Then, in Subsection II-C the CSI is given, which contains target range, Doppler and micro-Doppler information.

A. 5G NR TDD Configuration

The ISAC system proposed in this paper is based on the 5G New Radio (NR) protocol. The 5G NR basic resource unit in the time domain is the radio frame, with each radio frame lasting for 10 ms and consisting of 10 subframes, each with a duration of 1 ms. With the subcarrier spacing of 30 kHz, each subframe contains 2 slots and each slot contains 14 orthogonal frequency division multiplexing (OFDM) symbols. In the TDD mode, there are three types of slots between BS and UE: downlink (DL) slots, flexible slots and uplink (UL) slots. DL slots are used for broadcasting by the BS and transmitting control information and communication data to UE. The flexible slots serve as intervals for switching between UL and DL transmissions. UL slots are used for UE feedback and information reporting to BS.

Micro-Doppler feature extraction requires the sensing symbols in the ISAC system to be sufficiently dense. Therefore, we consider a frame structure designed for UAV micro-Doppler feature extraction as shown in Fig. 1 (b). During DL slots, the BS utilizes all Physical Downlink Shared Channel (PDSCH) signals as sensing symbols, resulting in the shortest pulse repetition interval (PRI) of $33.3 \mu\text{s}$. Currently, BS operates in a TDD mode with a single cycle duration of 2.5 ms, i.e. "DDDSU", as the ISAC mode. After BS detects an unknown flying target, it transmits communication signals to the target

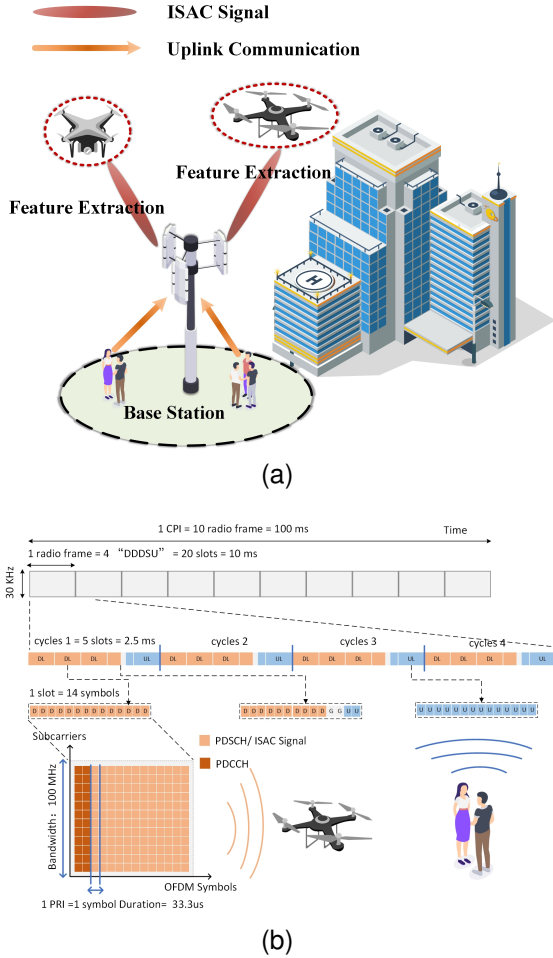


Fig. 1: Low altitude UAV identification scenario and frame structure configuration: (a) Urban low altitude UAV identification scenario. (b) TD-ISAC Configuration.

in the DL slots while simultaneously receiving echoes. In this sensing mode, the extracted micro-Doppler features are unambiguous.

B. Received Signal Model

In sensing applications, we select several radio frames as one coherent processing interval (CPI). During a single CPI, the BS transmits a total of M PDSCH OFDM symbols during DL slots. The transmitted baseband signal $s(t)$ within a single CPI is expressed as

$$s(t) = \sum_{m=1}^M \sum_{n=1}^N \mathbf{D}_{\text{TX}}(n, m) \times \exp(j2\pi n \Delta f t) \text{rect}\left(\frac{t - mT_s}{T_s}\right), \quad (1)$$

where N denotes the number of subcarriers. $\mathbf{D}_{\text{TX}} \in \mathbb{C}^{N \times M}$ represents the resource grid that transmits signals and $\mathbf{D}_{\text{TX}}(n, m)$ is the m symbol modulated on the n subcarrier, also called the complex modulation symbol. Δf is the subcarrier interval and $T_s = \frac{1}{\Delta f} + T_g$ denotes the total duration

of one OFDM symbol including that of the cyclic prefix (CP). T_g , $\text{rect}(\cdot)$ is a rectangular window of unity support.

The ISAC transmission signal propagates in free space and is reflected by the target. The transmitted signal in the time domain is $s(t) \exp(j2\pi f_c t)$ and f_c represents the central frequency of the transmitter. Considering that there is a strong scattering point in the echos, the received signal $\tilde{y}(t, R(t), \gamma(t))$ at the receiving end is

$$\tilde{y}(t, R(t), \gamma(t)) = \gamma(t) s\left(t - \frac{2R(t)}{c}\right) \exp(j2\pi f_c t) \times \exp\left(-j2\pi f_c \frac{2R(t)}{c}\right), \quad (2)$$

where $\gamma(t)$ is the channel attenuation and $R(t)$ is the distance from the scattering point to the BS.

Scatterers on the UAV have different motion characteristics and scattering intensity characteristics. The scatterers from the rotor exhibit both translational and rotational motions. The rotational motion causes dynamic variations in the RCS, leading to time-varying scattering intensities [27]. The scatterers from the UAV body exhibit both translational and vibrational motions [29]. The analysis is as follows.

The geometry of the ISAC BS and the UAV rotor is shown in Fig. 2. For simplicity, the UAV is composed by a set of point scatterers, which are the primary reflecting points on the target. The target depicted in Fig. 2 represents one of the UAV blades. The BS is located at the origin (X, Y, Z) of the space-fixed coordinates. The rotor is described in a local coordinate system (x, y, z) that is attached to the target and has translation and rotation with respect to the BS coordinates. To observe the rotation of the rotor, a reference coordinates (X', Y', Z') is introduced, which shares the same origin with the target but no rotation with respect to the BS coordinates. The distance from the BS to the UAV origin is R_0 . The azimuth and elevation angles of the reference coordinate origin observed by the BS are α and θ , respectively.

The rotor has a translation velocity v relative to the BS and rotates around the Z -axis with a rotational speed of f_r . Thus, a point scatterer p in the UAV rotor at time $t = 0$ will move to p'' at time t . The movement consists of two steps: (1) translation from p to p' , as shown in Fig. 2, with a velocity v ; and (2) rotation from p' to p'' with a rotational speed of f_r . The modeling of the motion characteristics and scattering properties of different scatterers on the UAV is as follows:

1) *UAV Body Translation*: The body of the UAV can be regarded as a strong scattering point. The radial motion pattern of the scatterer on the body, representing translational movement relative to the BS, is as follows:

$$R_{\text{trans}}^{\text{body}}(t) = R_0 + vt. \quad (3)$$

During a single CPI, the radial motion distance of the UAV is very short. Hence, its scattering intensity $\gamma^{\text{body}}(t)$ can be considered as a constant γ^{body} . Therefore, the echo from the scatterer due to the translational motion of the body can be expressed as

$$y_{\text{trans}}^{\text{body}}(t) = \tilde{y}\left(t, R_{\text{trans}}^{\text{body}}(t), \gamma^{\text{body}}\right). \quad (4)$$

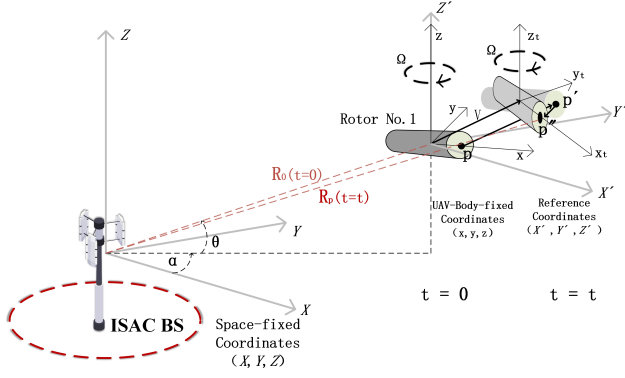


Fig. 2: Geometry of the BS and the UAV first rotor with translation and rotation.

2) *UAV Rotor Rotation*: Each UAV is equipped with multiple blades, one of which is illustrated in Fig. 2. Ignoring the distance from the UAV blade tip to the UAV body. Let azimuth angle $\alpha = 0$, the distance from the BS to the scatter point p (at the tip of the blade) can be expressed as

$$R_p^{\text{rotor}}(t) = R_0 + vt + \frac{L}{2} \cos \theta \cos(2\pi f_r t + \varphi_p), \quad (5)$$

where L is the length of the blade, and $(L/R_0)^2 \rightarrow 0$ in the far field. φ_p represents the initial rotation angle of the scattering point p on the blade.

The high-speed rotation of the blades results in a dynamic RCS [35]. To simplify matters, we can allocate the RCS of each blade to the blade's tip [27]. The RCS of scatterer p at time t can be expressed as

$$\sigma_p^{\text{rotor}}(t) = \sum_{\ell=1}^{\infty} \sum_{i=1}^I a_i \sin \left[b_i \frac{f_r}{100} \left(t + \frac{\varphi_p}{2\pi f_r} \right) + c_i \right] \times u_1 \left(t - \frac{\ell}{f_r} + \frac{\varphi_p}{2\pi f_r} \right), \quad (6)$$

where

$$u_1(t) = \begin{cases} 1, & 0 \leq t < \frac{1}{f_r} \\ 0, & t > \frac{1}{f_r} \end{cases}, \quad (7)$$

and I varies according to the material of the UAV blades. a_i, b_i and c_i represent the coefficients under different materials, respectively. Within a single CPI, this dynamic RCS results in rapid variations in the scattering intensity $\gamma_p^{\text{rotor}}(t)$. Considering multiple scatterers on multiple rotors, the echo from the scatterers due to the rotor rotation can be expressed as

$$y_{\text{rotation}}^{\text{rotor}}(t) = \sum_{p=1}^P \tilde{y}(t, R_p^{\text{rotor}}(t), \gamma_p^{\text{rotor}}(t)), \quad (8)$$

where P represent the total number of blades.

3) *UAV Body Vibration*: In practical applications, due to the interaction between the UAV body and the air, the UAV body has some high-frequency vibration components, which are added to the echoes from the target [36]. The vibration components also generate micro-Doppler signals, which adversely affects the extraction of rotor micro-Doppler signal features.

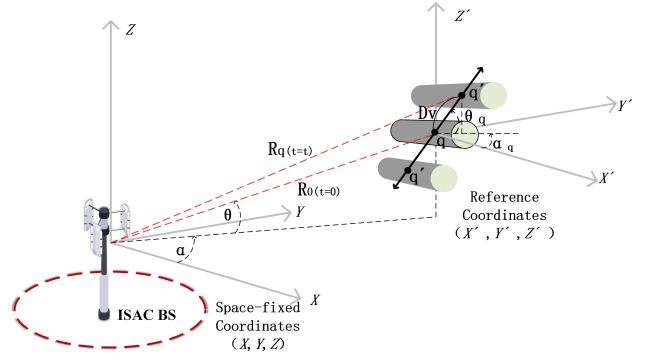


Fig. 3: Geometry of the BS and the UAV vibration.

Assume that the scatter q in the body of the UAV vibrates at a frequency f_v with an amplitude D_v and that the azimuth and elevation angle of the vibration direction in the reference coordinates (X', Y', Z') are α_q and θ_q , respectively, as shown in Fig. 3. If the azimuth angle α and the elevation angle θ_q of the scatter q are all zero, then we have

$$R_q^{\text{body}}(t) = R_0 + vt + D_v \sin(2\pi f_v t) \cos \theta \cos \alpha_q. \quad (9)$$

The vibration of the UAV body has a minimal impact on the RCS [26]. Therefore, the scattering intensity of this scatterer $\gamma_q^{\text{body}}(t)$ can also be considered as a constant γ_q^{body} . The echo from the scatterer due to the vibration motion of the body can be expressed as

$$y_{\text{vibration}}^{\text{body}}(t) = \tilde{y}(t, R_q^{\text{body}}(t), \gamma_q^{\text{body}}). \quad (10)$$

The total scattering echo of the UAV is given by the coherent sum of all independent scattering centers at that instant,

$$y(t) = y_{\text{trans}}^{\text{body}}(t) + y_{\text{vibration}}^{\text{body}}(t) + y_{\text{rotation}}^{\text{rotor}}(t) + n(t), \quad (11)$$

where $n(t)$ is additive white Gaussian noise (AWGN) with variance of σ_n^2 .

C. UAV CSI Model

The signal in (11) is sampled at the receiver with the period of T_s . Therefore, the sampled echo can be expressed as $y(t_m)$, where $t_m = mT_s \in \{T_s, 2T_s, \dots, MT_s\}$ represents the discrete time. After RF (radio frequency) demodulation and OFDM demodulation, according to (1) and (11), the signal expression on the resource grid at the receiver is,

$$\mathbf{D}_{\text{RX}}(n, m) = \mathbf{D}_{\text{TX}}(n, m) \mathbf{\Theta}(n, m) + \mathbf{\Omega}(n, m), \quad (12)$$

where $\mathbf{D}_{\text{RX}} \in \mathbb{C}^{N \times M}$. $\mathbf{\Omega}(n, m)$ represents Gaussian white noise. The matrix $\mathbf{\Theta} = \mathbf{k}_R \otimes \mathbf{k}_D$, where $\mathbf{k}_R \in \mathbb{C}^{N \times 1}$ carries the range information of the target, and $\mathbf{k}_D \in \mathbb{C}^{1 \times M}$ carries the Doppler and micro-Doppler information of the target. $\mathbf{k}_R(n)$ and $\mathbf{k}_D(m)$ are modeled as follows:

$$\mathbf{k}_R(n) = \exp \left(-j2\pi n \Delta f \frac{2R_0}{c} \right), n = 1, 2, \dots, N, \quad (13)$$

$$\mathbf{k}_D(m) = \mathbf{k}_D^{\text{trans}}(m) + \mathbf{k}_{mD}^{\text{vibration}}(m) + \mathbf{k}_{mD}^{\text{rotation}}(m), \quad m = 1, 2, \dots, M, \quad (14)$$

where $\mathbf{k}_D^{\text{trans}} \in \mathbb{C}^{1 \times M}$ represents the Doppler phase information due to the translational motion of the UAV body. $\mathbf{k}_{mD}^{\text{vibration}} \in \mathbb{C}^{1 \times M}$ represents the micro-Doppler phase information due to the body vibration, and $\mathbf{k}_{mD}^{\text{rotation}} \in \mathbb{C}^{1 \times M}$ represents the micro-Doppler amplitude-phase information due to the rotor rotation. The representations of $\mathbf{k}_D^{\text{trans}}$, $\mathbf{k}_{mD}^{\text{vibration}}$ and $\mathbf{k}_{mD}^{\text{rotation}}$ are as follows:

$$\begin{aligned} \mathbf{k}_D^{\text{trans}}(m) &= \gamma^{\text{body}} \exp(-j2\pi f_D(m)), \\ \mathbf{k}_{mD}^{\text{vibration}}(m) &= \gamma^{\text{body}} \exp(-j2\pi(f_D(m) + f_{mD}^v(m))), \\ \mathbf{k}_{mD}^{\text{rotation}}(m) &= \sum_{p=1}^P \gamma_p^{\text{rotor}}(m) \\ &\quad \exp(-j2\pi(f_D(m) + f_{mD}^p(m))), \\ &\quad m = 1, 2, \dots, M, \end{aligned} \quad (15)$$

where $f_D(m) = \frac{2vmT_s}{\lambda}$ represents the Doppler effect caused by the translational motion. $f_{mD}^v(m) = \frac{2D_v \cos \theta \cos \alpha_g \sin(2\pi f_v m T_s)}{\lambda}$ represents the micro-Doppler effect caused by the vibration, and $f_{mD}^p(m) = \frac{L \cos \theta \cos(2\pi f_r m T_s + \varphi_p)}{\lambda}$ represents the micro-Doppler effect caused by the rotor rotation.

Divide the corresponding elements of the transmitted signal on the resource grid to eliminate the influence of the amplitude and phase of the data. The signal model of the CSI containing target motion information is established as follows:

$$\text{CSI}(n, m) = \frac{\mathbf{D}_{\text{RX}}(n, m)}{\mathbf{D}_{\text{TX}}(n, m)} = \Theta(n, m) + \Omega'(n, m). \quad (16)$$

III. UAV ROTOR FEATURE EXTRACTION ALGORITHM

In this section, we present a method for extracting UAV micro-Doppler features using ISAC BS. The overall process is illustrated in Fig. 4. First, in Subsection III-A, we introduce the matched filtering method to determine the position of the UAV and give the mixed signal model to be decomposed. Then in Subsection III-B, an operator-based signal decomposition method, denoted by rmD-NSP, is adopted to extract the rotor micro-Doppler signals from the mixed signals. Finally, in Subsection III-C, the feature extraction method, denoted by SET, is applied to obtain the high resolution rotor features from the decomposed signals.

A. Determine the UAV position

According to (13) and (16), the range R_0 between the UAV and the BS can be obtained by performing an inverse discrete Fourier transform (IDFT) along the columns of the CSI matrix. The matrix after IDFT processing is denoted as **TRM**:

$$\mathbf{TRM} = \begin{pmatrix} \mathbf{d}(1) \mathbf{k}_D(1) & \mathbf{d}(1) \mathbf{k}_D(2) & \cdots & \mathbf{d}(1) \mathbf{k}_D(M) \\ \mathbf{d}(2) \mathbf{k}_D(1) & \mathbf{d}(2) \mathbf{k}_D(2) & \cdots & \mathbf{d}(2) \mathbf{k}_D(M) \\ \vdots & \vdots & \ddots & \vdots \\ \mathbf{d}(N) \mathbf{k}_D(1) & \mathbf{d}(N) \mathbf{k}_D(2) & \cdots & \mathbf{d}(N) \mathbf{k}_D(M) \end{pmatrix}, \quad (17)$$

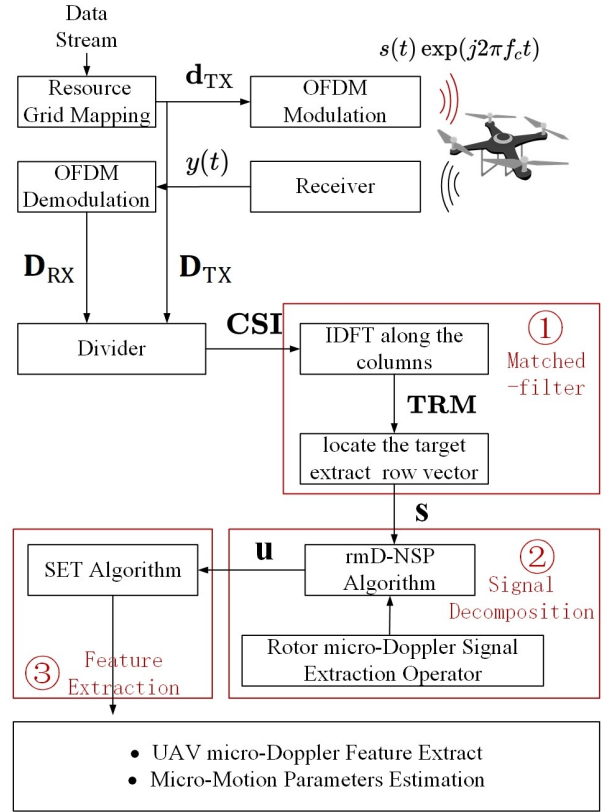


Fig. 4: Overall procedure of UAV feature extraction.

where $\mathbf{TRM} \in \mathbb{C}^{N \times M}$, and $\mathbf{d} \in \mathbb{C}^{N \times 1}$ is given by,

$$\begin{aligned} \mathbf{d}(k) &= \text{IDFT}[\mathbf{k}_R(n)] = \frac{1}{N} \sum_{n=1}^N \mathbf{k}_R(n) \exp\left(j \frac{2\pi}{N} nk\right) \\ &= \frac{1}{N} \sum_{n=1}^N \exp\left(-j2\pi n \Delta f \frac{2R_0}{c}\right) \exp\left(j \frac{2\pi}{N} nk\right), \\ &\quad k = 1, \dots, N. \end{aligned} \quad (18)$$

When the UAV is present, $|\mathbf{d}|$ will exhibit a peak. Let $k_p \in \{1, 2, \dots, N\}$ denote the position where the peak appears. Then, we extract the k_p -th row vector, denoted by $\mathbf{s}_{\text{uav}} \in \mathbb{C}^{1 \times M}$, from the **TRM**,

$$\mathbf{s}_{\text{uav}} = \mathbf{TRM}(k_p, :) = \mathbf{d}(k_p) \mathbf{k}_D. \quad (19)$$

In actual urban environments, the echoes contain not only the target but also significant strong interfering clutter. Considering this, the mixed signal model $\mathbf{s}_{\text{mix}} \in \mathbb{C}^{M \times 1}$ to be decomposed is formulated as follows:

$$\mathbf{s}_{\text{mix}} = \mathbf{s}_{\text{uav}}^T + \boldsymbol{\eta}_c, \quad (20)$$

where $\boldsymbol{\eta}_c \in \mathbb{C}^{M \times 1}$ represents the clutter and noise vector.

According to (14) and (20), \mathbf{s}_{mix} contains the body Doppler information $\mathbf{k}_D^{\text{trans}}$, the body vibration micro-Doppler information $\mathbf{k}_{mD}^{\text{vibration}}$, the micro-Doppler information $\mathbf{k}_{mD}^{\text{rotation}}$ caused by the rotation of the rotors and the clutter. Meanwhile, if the micro-Doppler feature extraction processing is directly performed on \mathbf{s}_{mix} , the resulting time-frequency spectrogram

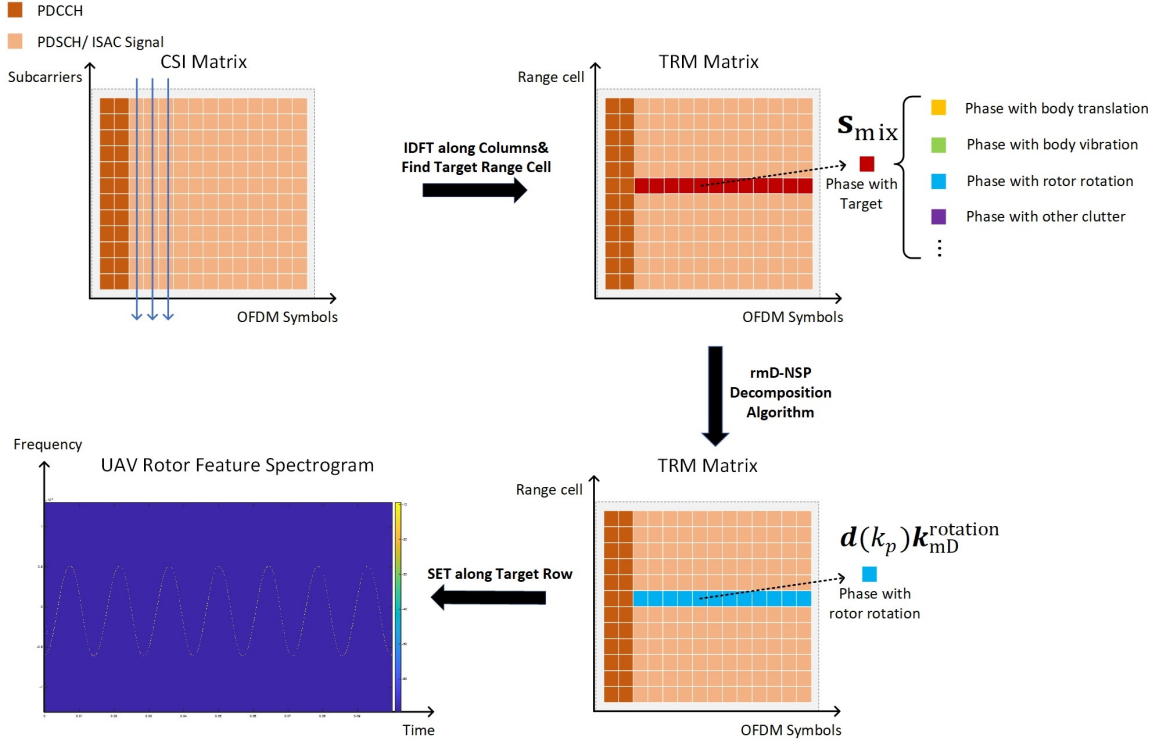


Fig. 5: The objective of the decomposition algorithm.

not only contains the rotor micro-Doppler features but also includes significant interference information. The micro-Doppler signals generated by the body vibration overlap with the rotor micro-Doppler signals, affecting the feature extraction results [29]. Moreover, the weak rotor micro-Doppler signals are obscured by strong interference signals such as clutter and echoes from the UAV body.

According to (6) and (15), the unique motion characteristics of the rotors modulate the echo in both amplitude and phase. Our approach is to leverage the distinctive amplitude-phase information of the rotor micro-Doppler signals $\mathbf{k}_{mD}^{\text{rotation}}$ to separate them from the mixed signal \mathbf{s}_{mix} using a signal decomposition method. Subsequently, feature extraction processing is performed on the decomposed signal.

B. Operator-based Signal Decomposition Algorithm

In Section III-A, we obtain a mixed signal \mathbf{s}_{mix} that includes the rotor micro-Doppler signals $\mathbf{d}(k_p)\mathbf{k}_{mD}^{\text{rotation}}$ along with various interference signals. Our goal is to obtain $\mathbf{d}(k_p)\mathbf{k}_{mD}^{\text{rotation}}$ from \mathbf{s}_{mix} to extract the UAV rotor micro-Doppler features as shown in Fig. 5. This is essentially a multi-component signal decomposition problem. Several multi-component signal decomposition algorithms have been studied, such as empirical mode decomposition (EMD) and variational mode decomposition (VMD) [37], [38]. However, EMD and VMD do not perform signal decomposition based on the form of the target signal, making them unsuitable for decomposing mixed signal \mathbf{s}_{mix} to extract the micro-Doppler signals.

Null space pursuit (NSP) is an adaptive operator-based signal decomposition method that constructs adaptive operators

to remove local narrowband signals in the zero space for separation [30]–[32]. The main appeal of this algorithm lies in its ability to design an adaptive operator based on the target signal model, enabling the extraction of the target signal from the mixed signal. The algorithm implementation consists of two main steps: (i) Design a parameterized operator based on the form of the target signal. (ii) Use null-space tracking to adaptively adjust the operator parameters while simultaneously extracting the target signal. In this paper, the target signal is the rotor micro-Doppler signal $\mathbf{d}(k_p)\mathbf{k}_{mD}^{\text{rotation}}$. By designing the specific operator, we can achieve effective separation of the target signal.

1) *Parameterized Operator Design.*: Specifically, the NSP algorithm leverages the prior information about the target signal. It designs adaptive operators based on the mathematical representation of the target signal, ensuring that the target signal falls into the zero space of the operator.

By observing the mathematical representation of rotor micro-Doppler signal $\mathbf{d}(k_p)\mathbf{k}_{mD}^{\text{rotation}}$ and according to (6), we can see that $\mathbf{d}(k_p)\mathbf{k}_{mD}^{\text{rotation}}$ is composed of the product of an amplitude term and a phase term, where the phase term includes linearly time-varying Doppler information $f_D(m)$ and non-linearly time-varying micro-Doppler information $f_{mD}^p(m)$ in their frequency modulation. Furthermore, due to the dynamic RCS characteristics caused by the high-speed rotation of the blades, rotor micro-Doppler signal also exhibits amplitude modulation $\gamma_p^{\text{rotor}}(m)$ according to (6), where the modulation frequency is related to the rotational speed. Therefore, our idea is to utilize the unique amplitude-phase information of rotor signal to construct an operator \mathcal{T}_{mD} , ensuring that $\mathbf{d}(k_p)\mathbf{k}_{mD}^{\text{rotation}}$ falls into the null space of this

operator.

In actual hardware processing, the signal is divided into real and imaginary parts for separate acquisition. The operator \mathcal{T}_{mD} thus effectively process on the real and imaginary parts of the signal. The operator processes both the real and imaginary components of the signal in an identical manner. Here, we take the real part as an example,

$$\mathcal{T}_{mD} \left(\Re \left\{ \mathbf{d}(k_p) \mathbf{k}_{mD}^{\text{rotation}}(m) \right\} \right) = 0. \quad (21)$$

According to (15), the real part of rotor micro-Doppler signal $\Re \left\{ \mathbf{d}(k_p) \mathbf{k}_{mD}^{\text{rotation}}(m) \right\}$ can be simplified to $a(m) \cos(\phi_1(m) + \phi_2(m))$, where $a(m) = \Re \left\{ \mathbf{d}(k_p) \gamma_p^{\text{rotor}}(m) \right\}$ contains amplitude modulation information, varying with changes in RCS, $\phi_1(m) = f_{mD}^p(m)$ represents micro-Doppler information, $\phi_2(m) = f_D(m)$ represents Doppler information.

Typically, for signals of this form, a second-order differential parameterized operator \mathcal{T}_{mD} is chosen to extract the target signal [31]:

$$\mathcal{T}_{mD} = \mathcal{D}_2 + \mathbf{p}(m) \mathcal{D}_1 + \mathbf{q}(m), \quad (22)$$

where \mathcal{D}_2 is defined as the second-order difference operator and \mathcal{D}_1 is defined as the first-order difference operator. $\mathbf{p} \in \mathbb{R}^{M \times 1}$ and $\mathbf{q} \in \mathbb{R}^{M \times 1}$ are the parameters of the operator.

We substitute the simplified target signal expressions into (21),

$$\mathcal{T}_{mD} (a(m) \cos(\phi_1(m) + \phi_2(m))) = 0. \quad (23)$$

According to (23), the expressions for the parameters $\mathbf{p}(m)$ and $\mathbf{q}(m)$ in the operator \mathcal{T}_{mD} can be derived. Due to the extremely small sampling interval T_s , the derivative of the sampled discrete-time sequence with respect to time closely approximates the derivative of the actual continuous-time form. Let $x'(m) \triangleq \frac{dx(t)}{dt} \big|_{t=mT_s}$, $x''(m) \triangleq \frac{d^2x(t)}{dt^2} \big|_{t=mT_s}$, and $\bar{\phi}(m) = \phi_1'(m) + \phi_2'(m)$, the following equation is given:

$$\begin{cases} -2a'(m) \bar{\phi}(m) - a(m) (\bar{\phi}'(m) - \bar{\phi}(m) \mathbf{p}(m)) = 0, \\ a''(m) + a'(m) \mathbf{p}(m) + a(m) (\mathbf{q}(m) - \bar{\phi}^2(m)) = 0. \end{cases} \quad (24)$$

Since $\phi_2(m)$ is a linear first-order function of m , $\phi_2''(m) = 0$. Then we obtain the expressions for $\mathbf{p}(m)$ and $\mathbf{q}(m)$:

$$\begin{cases} \mathbf{p}(m) = -2 \frac{a'(m)}{a(m)} - \frac{\phi_1''(m)}{\phi_1(m)}, \\ \mathbf{q}(m) = \bar{\phi}(m)^2 + 2 \left(\frac{a'(m)}{a(m)} \right)^2 + \frac{a'(m)}{a(m)} \frac{\phi_1''(m)}{\phi_1(m)} - \frac{a''(m)}{a(m)}, \end{cases} \quad (25)$$

where $\left| \frac{a'(m)}{a(m)} \right|$ is the instantaneous bandwidth of the signal.

We assume that $\bar{\phi}(m)^2 + 2 \left(\frac{a'(m)}{a(m)} \right)^2 + \frac{a'(m)}{a(m)} \frac{\phi_1''(m)}{\phi_1(m)} \gg \frac{a''(m)}{a(m)}$ according to [32]. Then we obtain the operator \mathcal{T}_{mD} ,

$$\begin{aligned} \mathcal{T}_{mD} = & \mathcal{D}_2 + \left(-2 \frac{a'(m)}{a(m)} - \frac{\phi_1''(m)}{\phi_1(m)} \right) \mathcal{D}_1 \\ & + \bar{\phi}(m)^2 + 2 \left(\frac{a'(m)}{a(m)} \right)^2 + \frac{a'(m)}{a(m)} \frac{\phi_1''(m)}{\phi_1(m)}. \end{aligned} \quad (26)$$

At this point, the real part of the rotor micro-Doppler signal is in the null space of the designed operator. The operator design is complete.

2) *Null Space Pursuit Algorithm*: According to the NSP theory, after designing the operator \mathcal{T}_{mD} specific to the real part of target signal, the following optimization problem can be solved to estimate the parameters of the operator, and separate the real part of the mixed signal $\mathbf{s}_{\text{real}} = \Re\{\mathbf{s}_{\text{mix}}\} \in \mathbb{R}^{M \times 1}$ into the target signal $\mathbf{u} = \mathbf{s}_{\text{real}} - \mathbf{r} \in \mathbb{R}^{M \times 1}$ and the residual $\mathbf{r} \in \mathbb{R}^{M \times 1}$,

$$\begin{aligned} & \min_{\mathbf{r}(m), \mathbf{p}(m), \mathbf{q}(m), \lambda_1, \gamma} \left\{ \|\mathcal{T}_{mD}(\mathbf{s}_{\text{real}}(m) - \mathbf{r}(m))\|^2 \right. \\ & + \lambda_1 (\|\mathbf{r}(m)\|^2 + \gamma \|\mathbf{s}_{\text{real}}(m) - \mathbf{r}(m)\|^2) \\ & \left. + \lambda_2 (\|\mathcal{D}_2 \mathbf{q}(m) + \mathbf{p}(m)\|^2) \right\}, \end{aligned} \quad (27)$$

where λ_1 and λ_2 are the Lagrange multiplier. γ is the leakage parameter determining the quantity of $\mathbf{s}_{\text{real}}(m) - \mathbf{r}(m)$ preserved in the null space of \mathcal{T}_{mD} .

We obtain the matrix form of corresponding augmented Lagrangian function as expressed in (27),

$$\begin{aligned} \mathcal{F}(\mathbf{r}, \boldsymbol{\theta}, \lambda_1, \gamma) = & \|\mathbf{D}_2(\mathbf{s}_{\text{real}} - \mathbf{r}) + \mathbf{A}\boldsymbol{\theta}\|^2 \\ & + \lambda_1 (\|\mathbf{r}\|^2 + \gamma \|\mathbf{s}_{\text{real}} - \mathbf{r}\|^2) \\ & + \lambda_2 \|\mathbf{M}_2 \boldsymbol{\theta}\|^2, \end{aligned} \quad (28)$$

where $\boldsymbol{\theta} = [\mathbf{p}^T, \mathbf{q}^T]^T \in \mathbb{R}^{2M \times 1}$ contains the operator parameters. $\mathbf{A} = \begin{bmatrix} \mathbf{A}_{\mathbf{D}_1(\mathbf{s}_{\text{real}} - \mathbf{r})} & \mathbf{A}_{\mathbf{s}_{\text{real}} - \mathbf{r}} \end{bmatrix} \in \mathbb{R}^{M \times 2M}$. $\mathbf{M}_2 = [\mathbf{D}_2 \quad \mathbf{E}] \in \mathbb{R}^{M \times 2M}$, where $\mathbf{E} \in \mathbb{R}^{M \times M}$ is the identity matrix. $\mathbf{D}_2 \in \mathbb{R}^{M \times M}$ and $\mathbf{D}_1 \in \mathbb{R}^{M \times M}$ can be written as follows, which represent the second-order differential matrix and the first-order differential matrix, respectively,

$$\mathbf{D}_2 = \begin{bmatrix} -1 & 1 & 0 & \cdots & 0 \\ 1 & -2 & 1 & \cdots & 0 \\ \vdots & \ddots & \ddots & \ddots & \vdots \\ 0 & \cdots & 1 & -2 & 1 \\ 0 & \cdots & 0 & 1 & -1 \end{bmatrix}, \quad (29)$$

$$\mathbf{D}_1 = \begin{bmatrix} -1 & 1 & 0 & \cdots & 0 \\ 0 & -1 & 1 & \cdots & 0 \\ \vdots & \ddots & \ddots & \ddots & \vdots \\ 0 & \cdots & 0 & -1 & 1 \\ 0 & \cdots & 0 & 0 & -1 \end{bmatrix}. \quad (30)$$

We can solve the above problems by using an iterative algorithm. By iteratively calculating the parameters \mathbf{r} , $\boldsymbol{\theta}$, λ_1 and γ , we can estimate the parameters of the operator \mathcal{T}_{mD} and extract the target micro-Doppler signal \mathbf{u} . In the j -th iteration, the current residual signal is \mathbf{r}^j , the current leakage component is γ^j , and the current Lagrangian parameters is λ_1^j . The specific parameter update process and sequence are as follows:

(1) *Iteration of $\boldsymbol{\theta}^j$* : The parameter $\boldsymbol{\theta}^j = [\mathbf{p}^{jT}, \mathbf{q}^{jT}]^T$ can be obtained by solving the following subproblem,

$$\boldsymbol{\theta}^j = \arg \min_{\boldsymbol{\theta}} \left\| \mathbf{D}_2(\mathbf{s}_{\text{real}} - \mathbf{r}^j) + \mathbf{A}^j \boldsymbol{\theta} \right\|^2 + \lambda_2 \|\mathbf{M}_2 \boldsymbol{\theta}\|^2, \quad (31)$$

where $\mathbf{A}^j = \begin{bmatrix} \mathbf{A}_{\mathbf{D}_1(\mathbf{s}_{\text{real}} - \mathbf{r}^j)} & \mathbf{A}_{\mathbf{s}_{\text{real}} - \mathbf{r}^j} \end{bmatrix}$. By setting the first derivatives of $\mathcal{F}(\mathbf{r}, \boldsymbol{\theta}, \lambda_1, \gamma)$ with respect to $\boldsymbol{\theta}$ to zero, we get

$$\hat{\boldsymbol{\theta}}^j = - \left(\mathbf{A}^{jT} \mathbf{A}^j + \lambda_2 \mathbf{M}_2^T \mathbf{M}_2 \right)^{-1} \mathbf{A}^{jT} \mathbf{D}_2 (\mathbf{s}_{\text{real}} - \mathbf{r}^j). \quad (32)$$

(2) *Iteration of λ_1^{j+1}* : The parameter λ_1^{j+1} is iteratively updated based on the NSP theory [30] which can be calculated as follows:

$$\lambda_1^{j+1} = \frac{1}{1 + \gamma^j} \frac{\mathbf{s}_{\text{real}}^T \chi^j \mathbf{s}_{\text{real}}}{\mathbf{s}_{\text{real}}^T \chi^j \mathbf{s}_{\text{real}}}, \quad (33)$$

where $\chi^j = \left(\mathbf{T}_{mD}^j \mathbf{T}_{mD}^j + (1 + \gamma^j) \lambda_1^j \mathbf{E} \right)^{-1}$ and $\mathbf{T}_{mD}^j = \mathbf{D}_2 + [\mathbf{A}_p \mathbf{A}_q] [\mathbf{D}_1^T \mathbf{E}^T]^T$.

(3) *Iteration of \mathbf{r}^{j+1}* : The parameter \mathbf{r}^{j+1} can be obtained by solving the following subproblem

$$\begin{aligned} \mathbf{r}^{j+1} = \arg \min_{\mathbf{r}} & \quad \|\mathbf{D}_2(\mathbf{s}_{\text{real}} - \mathbf{r}) + \mathbf{A}\boldsymbol{\theta}^j\|^2 \\ & + \lambda_1^{j+1} (\|\mathbf{r}\|^2 + \gamma^j \|\mathbf{s}_{\text{real}} - \mathbf{r}\|^2), \end{aligned} \quad (34)$$

by setting the first derivatives of $\mathcal{F}(\mathbf{r}, \boldsymbol{\theta}, \lambda_1, \gamma)$ with respect to \mathbf{r} to zero, we get

$$\begin{aligned} \mathbf{r}^{j+1} = & \left(\mathbf{T}_{mD}^j \mathbf{T}_{mD}^j + (1 + \gamma^j) \lambda_1^{j+1} \mathbf{E} \right)^{-1} \\ & \left(\mathbf{T}_{mD}^j \mathbf{T}_{mD}^j \mathbf{s}_{\text{real}} + \lambda_1^{j+1} \gamma^j \mathbf{s}_{\text{real}} \right). \end{aligned} \quad (35)$$

(4) *Iteration of γ^{j+1}* : The parameter γ^{j+1} can be iteratively updated according to the following equation [30]:

$$\gamma^{j+1} = \frac{(\mathbf{s}_{\text{real}} - \mathbf{r}^{j+1})^T \mathbf{s}_{\text{real}}}{\|\mathbf{s}_{\text{real}} - \mathbf{r}^{j+1}\|^2} - 1. \quad (36)$$

The value of the parameter λ_2 is less sensitive to the separation result which is set as a constant [30]. The detailed procedures are illustrated in Algorithm 1.

Algorithm 1 rmD-NSP to extract the micro-Doppler signal

Input: Mixed signal \mathbf{s}_{real} , stopping threshold ε and the initial values of λ_2 , λ_1^0 and γ^0 .

- 1: **Initialization:** Let $j = 0$, $\mathbf{r}^j = 0$, $\lambda_1^j = \lambda_1^0$ and $\gamma^j = \gamma^0$
- 2: **repeat**
- 3: $\boldsymbol{\theta}^j \leftarrow \mathbf{r}^j, \mathbf{A}^j$ according to (32).
- 4: $\lambda_1^{j+1} \leftarrow \lambda_1^j, \gamma^j, \boldsymbol{\theta}^j$ according to (33).
- 5: $\mathbf{r}^{j+1} \leftarrow \boldsymbol{\theta}^j, \gamma^j, \lambda_1^{j+1}$ according to (35).
- 6: $\gamma^{j+1} \leftarrow \mathbf{r}^{j+1}$ according to (36), and set $j = j + 1$.
- 7: **until** $\|\mathbf{r}^{j+1} - \mathbf{r}^j\|^2 > \varepsilon \|\mathbf{s}_{\text{real}}\|^2$

Output:

The extracted rotor micro-Doppler signal
 $\hat{\mathbf{u}} = (1 + \gamma^j) (\mathbf{s}_{\text{real}} - \mathbf{r}^j)$.

C. High-Resolution Feature Extraction Algorithm

After applying the rmD-NSP decomposition algorithm from the previous section, we have now extracted the rotor micro-Doppler component $\mathbf{d}(k_p) \mathbf{k}_{mD}^{\text{rotation}}$ from \mathbf{s}_{mix} . Next, we extract the micro-Doppler features of this signal. SET is a new time-frequency analysis method that can generate more energy-concentrated spectrogram results [33]. SET extracts time-frequency coefficients near the instantaneous frequency (IF) while discarding the remaining time-frequency coefficients, resulting in better performance for multi-component non-stationary signals. Therefore, we choose this algorithm as the method for subsequent feature extraction.

The main steps of this algorithm are:

(1) The decomposed signal \mathbf{u} after rmD-NSP algorithm retains most of the rotor micro-Doppler signals. Perform modified STFT on this signal:

$$\begin{aligned} S_{\mathbf{u}}(\eta, m) &= \sum_{\xi'=-\infty}^{+\infty} \mathbf{u}[\xi' + m] g^*[\xi'] e^{-2\pi j \eta \xi'} \\ &= \sum_{\xi=-\infty}^{+\infty} \mathbf{u}[\xi] g[\xi - m] e^{-2\pi j \eta (\xi - m)} \\ &= M_{\mathbf{u}}(\eta, m) e^{2j\pi \Phi_{\mathbf{u}}(\eta, m)}, \end{aligned} \quad (37)$$

where $g(m)$ is a finite-length window function, $M_{\mathbf{u}}(\eta, m)$ is the magnitude of STFT results, and $\Phi_{\mathbf{u}}(\eta, m)$ is the phase.

(2) Based on the modified STFT result $S_{\mathbf{u}}(\eta, m)$, we calculate the instantaneous frequency $\hat{\omega}_{\mathbf{u}}(\eta, m)$ of $\mathbf{u}(m)$ as follows:

$$\hat{\omega}_{\mathbf{u}}(\eta, m) = \begin{cases} \Re \left\{ \frac{\partial_m S_{\mathbf{u}}(\eta, m)}{2j\pi S_{\mathbf{u}}(\eta, m)} \right\}, & |S_{\mathbf{u}}(\eta, m)| > \gamma, \\ \infty, & |S_{\mathbf{u}}(\eta, m)| \leq \gamma, \end{cases} \quad (38)$$

where $\partial_m S_{\mathbf{u}}(\eta, m) \triangleq \frac{S_{\mathbf{u}}(\eta, m+1) - S_{\mathbf{u}}(\eta, m)}{T_s} \approx \left. \frac{dS_{\mathbf{u}}(\eta, t)}{dt} \right|_{t=mT_s}$. $\gamma > 0$ is to eliminate the unstable phenomenon or the influence of the noises.

(3) Perform energy extraction to obtain the SET result:

$$\begin{aligned} \text{SET}_{\mathbf{u}}(\eta, m) &= S_{\mathbf{u}}(\eta, m) \delta(\eta - \hat{\omega}_{\mathbf{u}}(\eta, m)) \\ &= \begin{cases} S_{\mathbf{u}}(\eta, m), & \eta = \hat{\omega}_{\mathbf{u}}(\eta, m) \\ 0, & \eta \neq \hat{\omega}_{\mathbf{u}}(\eta, m), \end{cases} \end{aligned} \quad (39)$$

where $\delta(\eta - \hat{\omega}_{\mathbf{u}}(\eta, m))$ is used to gather the STFT coefficients that have the same frequency to where they should appear.

IV. SIMULATION RESULTS

This section verifies the ability to extract UAV features using ISAC signal through software simulation. The simulation scenario is based on a DJI M300 RTK UAV and a Sub-6GHz BS, with the relative position of the BS and the UAV shown in Fig. 2. The UAV is modeled as a set of scatterers performs uniform linear motion along the radial direction of the BS. The scatterers on the rotor exhibit both translational and rotational motions, as shown in Fig. 2. The scatterers on the body exhibit both translational and vibrational motions, as shown in Fig. 3. The parameters for rotation and vibration are provided in Table I. Furthermore, these scatterers also have different scattering intensities, and σ^{body} is set to 0.1 m^2 , representing the RCS of the UAV body, which does not change with time over a short CPI. The RCS of the rotor blades can be assigned to the scatterers at the blade tips, denoted as $\sigma_p^{\text{rotor}}(t)$. The DJI M300 RTK is made of carbon fiber. According to [35], we set I in (6) and (7) to 6, and the specific coefficients a_i, b_i and c_i associated with the carbon fiber are given by

$$\begin{aligned} \mathbf{a} &= [1.133, 0.425, 0.7121, -0.1588, 0.1046, 0.0027], \\ \mathbf{b} &= [356.8, 1445, 608, 1946, 2236, 3513], \\ \mathbf{c} &= [-0.1997, -2.464, 1.695, 1.319, -0.1277, \\ & \quad -0.2433]. \end{aligned} \quad (40)$$

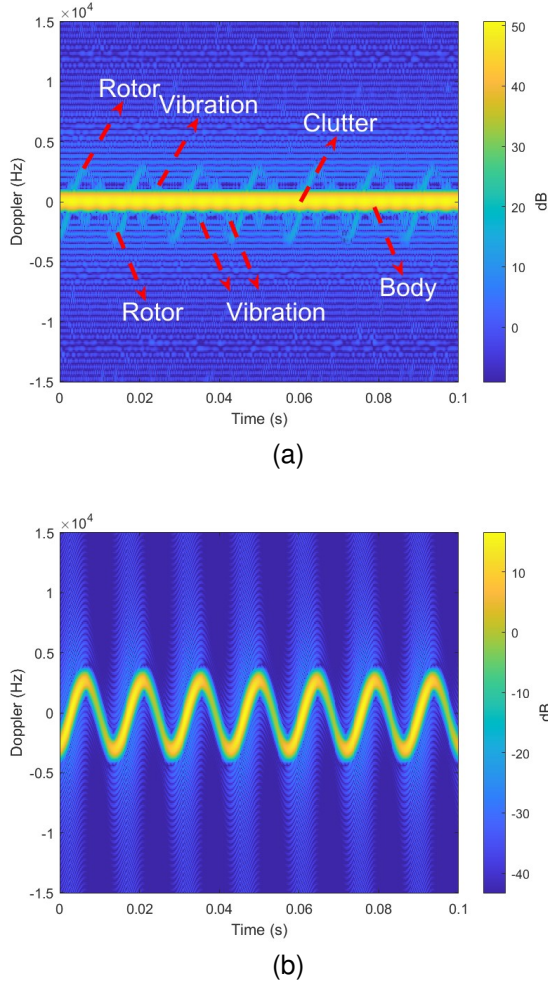


Fig. 6: UAV Spectrogram feature: (a) Spectrogram of micro-Doppler feature extraction from raw UAV echo. (b) Theoretical spectrogram of micro-Doppler feature extraction from UAV rotor.

Due to the high-speed rotation of the UAV blades, $\sigma_p^{\text{rotor}}(t)$ changes rapidly within the CPI. This causes the echo intensity from the UAV rotor blades to vary rapidly over time.

The scattering intensity $\gamma(t)$ is ultimately expressed using the received power in the radar equation [39], where P_t is the transmit power, set to 28 dBm [40]. G_t and G_r are the transmitting and receiving antenna gains, which are set to 18 dB, and λ is the wavelength. $\sigma(t)$ is related to the type of scatterer. For scatterers on the UAV body, this term can be approximated as $\sigma(t) \approx \sigma^{\text{body}}$, and for scatterers on the rotor blades, this term can be approximated as $\sigma(t) \approx \sigma_p^{\text{rotor}}(t)$. L_s is the system loss and can be ignored [39] and $L_a(R_0)$ is the path loss,

$$\gamma(t) = \frac{P_t G_t G_r \lambda^2 \sigma(t)}{(4\pi)^3 R^4 L_s L_a(R_0)}. \quad (41)$$

Let δ_r represent the system's range resolution, which is defined as follows:

$$\delta_r = \frac{c}{2B}, \quad (42)$$

TABLE I: SIMULATION PARAMETERS

Parameters	Symbol	Value
ISAC signal		PDSCH
Carrier frequency	f_c	3.5 GHz
Subcarrier spacing	Δf	30 kHz
Bandwidth	B	100 MHz
TDD frame structure		DDDSU
Duration of a OFDM symbol	T_s	36.6 μ s
Coherent processing interval		0.1 s
Number of downlink sensing symbols	M	1840
Number of subcarriers	N	3276
Total transmission power	P_t	28 dBm
Antenna gains	G_t, G_r	18 dB
Distance between the UAV and the BS	R_0	50 m
Azimuth angle	α	0 $^\circ$
Elevation angle	θ	30 $^\circ$
Velocity of the UAV	v	5 m/s
UAV rotation speed	f_r	80 r/s
Length of blade	L	0.5 m
Azimuth angle of vibration	α_q	10 $^\circ$
Elevation angle of vibration	θ_q	0 $^\circ$
Vibration frequency	f_v	100 Hz
Vibration amplitude	D_v	0.05 m
RCS of the UAV body	σ^{body}	0.1 m ²

where c represents the speed of light and B represents the system bandwidth. With a system bandwidth of 100 MHz, the range resolution δ_r is 1.5 m. In this case, all scattering points on the UAV fall within a single range cell, and the rotation of the rotor does not span multiple distance units. By extracting the range cell where the target is located and performing time-frequency analysis, the spectrogram of the UAV can be extracted as shown in Fig. 6 (a). The rotor micro-Doppler signals have a low intensity, and due to the presence of vibration components, the rotor micro-Doppler features are not clear. For comparison, Fig. 6 (b) shows the micro-Doppler feature with only one blade.

In order to extract the rotor micro-Doppler signals from the raw UAV echo, which contains numerous scatterers, and to obtain high-resolution rotor micro-Doppler characteristics, we apply three operator-based signal decomposition algorithms—NSP [30], AM-FM NSP [32], and the proposed rmD-NSP algorithm—on the mixed signal, i.e., s_{mix} described in (20). Subsequently, we use the SET method to extract the micro-Doppler feature from the decomposed signal. The results are shown in Fig. 7. The first row of Fig. 7 shows the results of decomposition and time-frequency feature enhancement using the rmD-NSP algorithm and SET. Fig. 7 (a) displays the results after the first decomposition, where the translation component of the UAV body and the stationary clutter are eliminated, but some vibration components have the same energy level as the rotor components, both being 5 dB. Fig. 7 (b) shows the final decomposition result of rmD-NSP. The rotor component exhibits a high energy level, reaching up to 5 dB, while the vibration component is only -20 dB. The rotor micro-Doppler characteristics are fully revealed from the environment, although the time-frequency ridge remains relatively coarse. Fig. 7 (c) shows the result of applying the SET to the final decomposition output of rmD-NSP, yielding a more refined time-frequency spectrogram. The second row of Fig. 7 shows the results of AM-FM NSP algorithm and SET

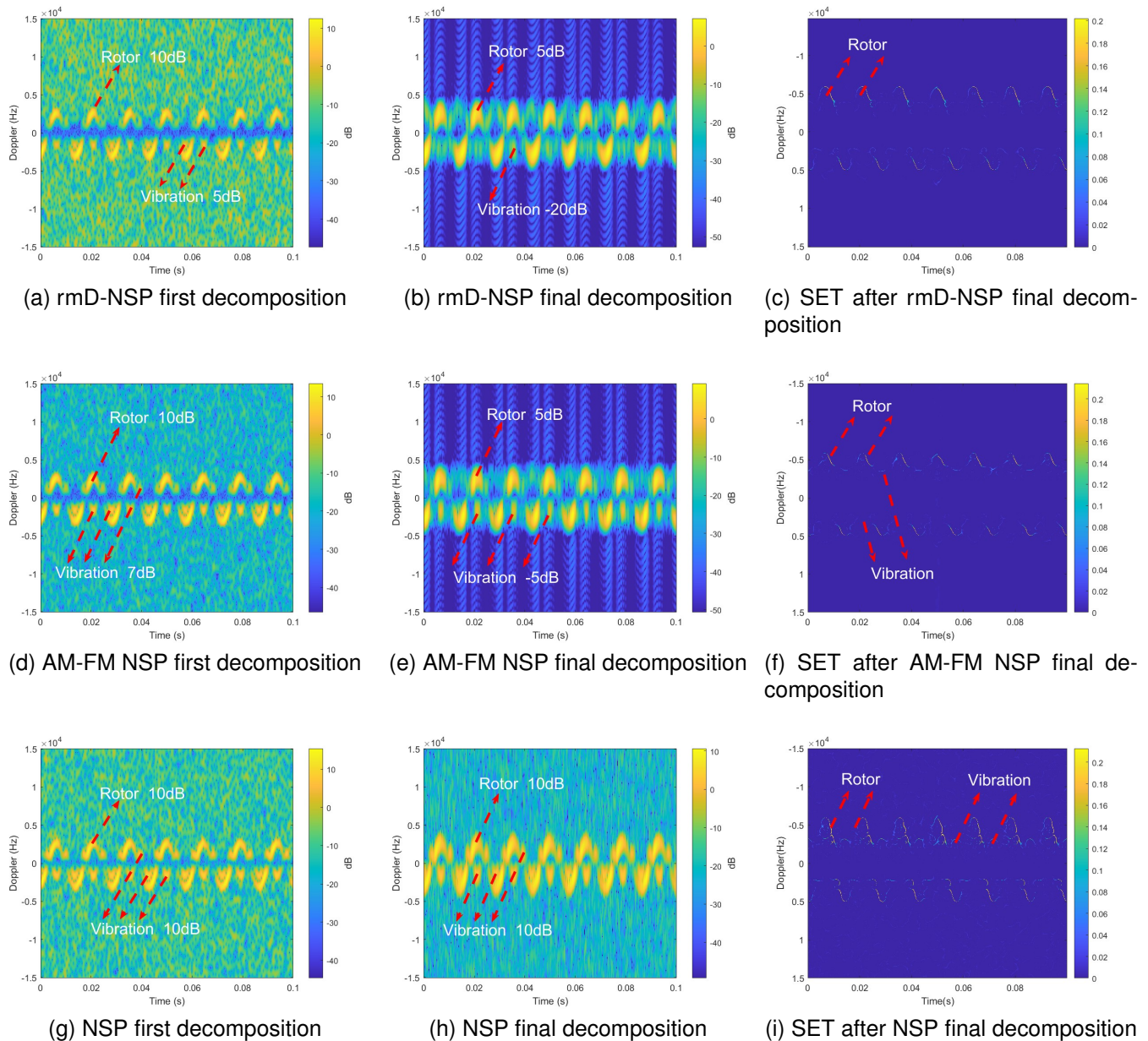


Fig. 7: Micro-Doppler feature extraction simulated by different methods. First row: (a) and (b) Spectrogram of the signals extracted using rmD-NSP, (c) spectrogram of the extracted signal using rmD-NSP after applying the SET algorithm. Second row: (d) and (e) Spectrogram of the signals extracted using AM-FM NSP [32], (f) spectrogram of the extracted signal using AM-FM NSP after applying the SET algorithm. Last row: (g) and (h) Spectrogram of the signals extracted using NSP [30], (i) spectrogram of the extracted signal using NSP after applying the SET algorithm.

algorithm. As shown in Fig. 7 (d), the first decomposition using the AM-FM NSP can still eliminate the UAV body Doppler and clutter components. Similar to rmD-NSP, it also retains some vibration components. Fig. 7 (e) shows the final decomposition result of AM-FM NSP, where it can be seen that some high-energy vibration components are still retained, reaching up to -5 dB, with energy levels close to those of the rotor. The last row of Fig. 7 shows the results of NSP and SET operations. From Fig. 7 (g) and Fig. 7 (h), it can be observed that the NSP algorithm consistently fails to eliminate

the vibration components. The final decomposition results still retain all the vibration components, with energy levels as high as 10 dB, matching that of the rotor. At this point, the time-frequency features on the spectrogram can no longer accurately represent the rotor's micro-Doppler features.

The reason for this issue is the difference in operators. First, the NSP operator only considers the frequency modulation component and has difficulty capturing the amplitude and frequency modulation components, such as the rotor's micro-Doppler signal. Therefore, during decomposition, it treats the vibration-induced micro-Doppler signal and the rotor-

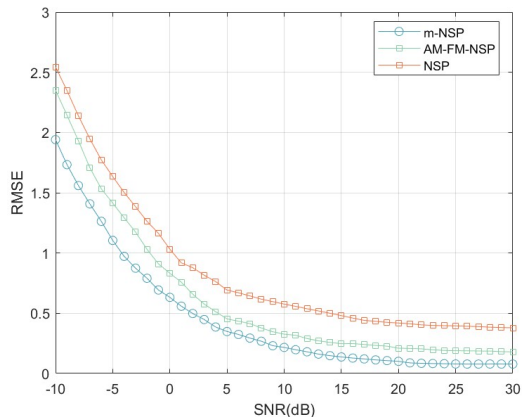


Fig. 8: RMSE under different SNRs for the different decomposition algorithm.

induced micro-Doppler signal as the same type of signal, resulting in residual vibration interference after decomposition. Both AM-FM NSP and rmD-NSP consider amplitude and frequency modulation components. However, rmD-NSP takes into account the characteristics of the rotor's micro-Doppler signal, with the frequency modulation component consisting of a linear Doppler term and a nonlinear micro-Doppler term according to (15). By utilizing this prior information, the algorithm can capture the differences between the vibration components and rotor components during the iterative decomposition process, resulting in better decomposition performance.



Fig. 9: UAV micro-Doppler extraction test scenario based on ISAC hardware testbed.

Further, we evaluate the decomposition performance of NSP, AM-FM NSP, and rmD-NSP algorithms on rotor micro-Doppler signals in a noisy environment. In this simulation, the mean-squared error (MSE) is used to assess the performance of NSP, AM-FM NSP, and rmD-NSP under noisy conditions. The signal-to-noise ratio (SNR) of the input signal increases in 1 dB increments from -10 dB to 30 dB. Fig. 8 presents the RMSE of the three algorithms in decomposing rotor micro-

Doppler signals. It can be observed that under a 30 dB SNR condition, the rmD-NSP algorithm performs better, achieving the smallest RMSE of only 0.07, compared to AM-FM NSP at 0.17 and NSP at 0.38. At a 5 dB SNR, the rmD-NSP algorithm still performs well with an RMSE of 0.34, compared to the other two algorithms.

$$\text{SNR} = \frac{\sum_{m=1}^M |s_{\text{uav}}(m)|^2}{M\sigma_n^2}, \quad (43)$$

V. HARDWARE TESTBED AND RESULTS

The proposed algorithm is verified on the Sub-6G ISAC hardware testbed. The ISAC system is based on the 5G NR protocol and consists of UL and DL baseband signal processing, intermediate frequency modulation, 3.5 GHz RF modulation, and antenna modules. The parameters for the Sub-6G ISAC hardware testbed are exactly the same as those listed in Table I. We utilize the proposed frame structure for sensing and communication functions. The test location is chosen in Ningbo, China, and the test scenario is shown in Fig. 9.

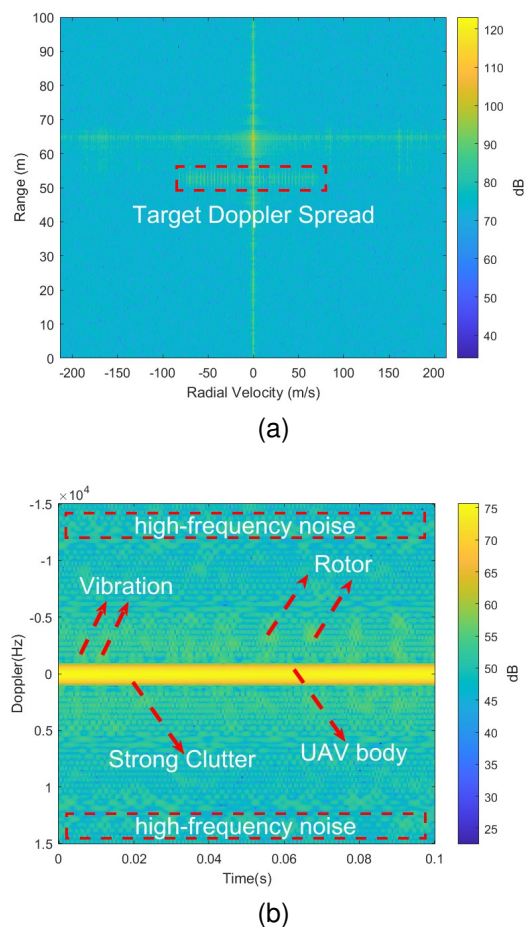


Fig. 10: Hardware testbed results: (a) Range-Doppler map of UAV. (b) Spectrogram of raw UAV echo.

The DJI M300 RTK UAV rotor length L is 0.5 m, and the body area is $0.26 \text{ m} \times 0.13 \text{ m}$. We controlled the UAV to fly uniformly along the radial direction of the BS at a speed of

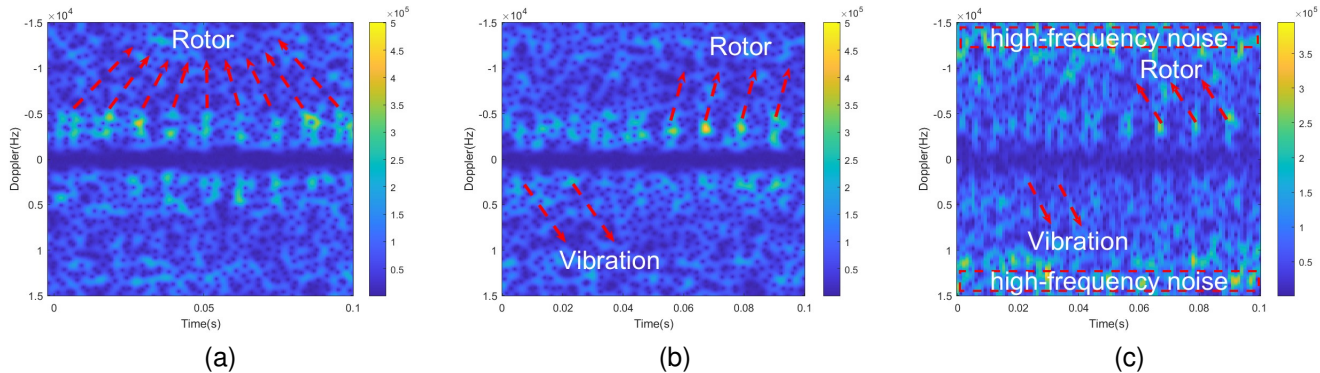


Fig. 11: Hardware testbed implementation results of the proposed algorithm: (a) Spectrogram after decomposition using the proposed rmD-NSP algorithm. (b) Spectrogram after decomposition using the AM-FM NSP algorithm [32]. (c) Spectrogram after decomposition using the NSP algorithm [30].

5 m/s, while the ISAC BS collected the echoes to obtain the target's CSI information. Performing 2D-FFT [41] on the CSI can obtain the range and Doppler information of the UAV, as shown in Fig. 10 (a). It can be seen that the UAV is not a point target on the range-Doppler map. At a distance of 53 m, it exhibits a Doppler spread of ± 90 m/s along the velocity axis, which is caused by the rotation of the rotor and the vibration of the UAV body. Fig. 10 (b) shows the result of performing a short-time Fourier transform (STFT) in the target range cell. It can be seen that there are many scattering points in the time-frequency spectrogram. Clutter and scatterers from the UAV body are present near the 0 Hz, with a very high intensity. Additionally, high-frequency noise originating from the hardware itself is present, with the intensity comparable to the rotor components. Consequently, the rotor micro-Doppler features are not prominent in the spectrogram.

We apply the proposed rmD-NSP, AM-FM NSP [32], and NSP [30] algorithms to extract the UAV rotor signals and perform SET on the extracted signals. The results are shown in Fig. 11. Fig. 11 (a) shows the results after applying the rmD-NSP decomposition. The spectrogram shows that the rotor micro-Doppler signals have high energy, clear features, and distinct periodicity. Within the 0.1 s observation period, eight rotations are clearly observed in the spectrogram, which is consistent with the software simulation results shown in Fig. 7 (b) and matches the actual rotational speed of 80 r/s for the DJI M300 RTK UAV. Additionally, the micro-Doppler frequency caused by the rotor rotation can reach approximately 4000 Hz, which also aligns with Fig. 7 (b). These demonstrate that the ISAC BS can accurately extract UAV's rotor micro-Doppler signals using the proposed algorithm in real urban scenarios. Fig. 11 (b) shows the results of extracting rotor signals using AM-FM NSP. The extraction quality is relatively low, capturing only 4-5 rotor rotations within the 0.1 s observation period, while retaining some low-frequency vibration components. Fig. 11 (c) shows that only three rotor rotations are extracted within the 0.1 s observation period. Additionally, the strength of the rotor components is comparable to that of the vibration components and high-frequency noise, indicating

the poorest extraction performance. The micro-Doppler feature extraction algorithm proposed in this paper can be utilized in complex urban environments. By leveraging Sub-6G base station, it effectively extracts features from rotor signals.

VI. CONCLUSION

In order to enable the base station to extract micro-Doppler features of aerial targets, this paper proposes a target feature extraction technique. We first considered a more realistic UAV scattering model, taking into account the vibration characteristics, high-speed rotor rotation, and dynamic RCS characteristics. Our goal is to extract the weak UAV's rotor micro-Doppler signals from complex environments and perform feature extraction. In the software simulation, we evaluated the effectiveness of the proposed rmD-NSP algorithm in extracting rotor micro-Doppler signals and compared it with the NSP and AM-FM NSP signal decomposition algorithms. We studied the decomposition performance of this method under different SNR. Additionally, we validated the algorithm with ISAC hardware testbed results. Using a Sub-6 GHz ISAC hardware testbed, we successfully extracted the rotor micro-Doppler signal and obtained high-resolution features. Within a 0.1 s observation period, ISAC BS successfully captures eight rotations of the DJI M300 RTK UAV's rotor in urban environment.

VII. ACKNOWLEDGMENT

The authors would like to express their sincere gratitude to Dr. Chunwei Meng and Dr. Kan Yu for their invaluable comments and suggestions, which have greatly improved the quality of this paper.

REFERENCES

- [1] H. Shakhathreh, A. H. Sawalmeh, A. Al-Fuqaha, Z. Dou, E. Almaita, I. Khalil, N. S. Othman, A. Khreishah, and M. Guizani, "Unmanned Aerial Vehicles (UAVs): A Survey on Civil Applications and Key Research Challenges," *IEEE Access*, vol. 7, pp. 48 572–48 634, 2019.
- [2] J. Watling and N. Reynolds, *Meatgrinder: Russian Tactics in the Second Year of Its Invasion of Ukraine*. Royal United Services Institute for Defence and Security Studies, 2023.

- [3] Y. Mekdad, A. Aris, L. Babun, A. El Fergougui, M. Conti, R. Lazeretti, and A. S. Ulugac, "A survey on security and privacy issues of UAVs," *Computer Networks*, vol. 224, p. 109626, 2023.
- [4] Y. Huang, Q. Wu, R. Lu, X. Peng, and R. Zhang, "Massive MIMO for cellular-connected UAV: Challenges and promising solutions," *IEEE Communications Magazine*, vol. 59, no. 2, pp. 84–90, 2021.
- [5] Y. Cui, Q. Zhang, Z. Feng, Q. Wen, Z. Wei, F. Liu, and P. Zhang, "Seeing is Not Always Believing: ISAC-Assisted Predictive Beam Tracking in Multipath Channels," *IEEE Wireless Communications Letters*, vol. 13, no. 1, pp. 14–18, 2024.
- [6] A. Zhang, M. L. Rahman, X. Huang, Y. J. Guo, S. Chen, and R. W. Heath, "Perceptive Mobile Networks: Cellular Networks With Radio Vision via Joint Communication and Radar Sensing," *IEEE Vehicular Technology Magazine*, vol. 16, no. 2, pp. 20–30, 2021.
- [7] A. Liu, Z. Huang, M. Li, Y. Wan, W. Li, T. X. Han, C. Liu, R. Du, D. K. P. Tan, J. Lu, Y. Shen, F. Colone, and K. Chetty, "A Survey on Fundamental Limits of Integrated Sensing and Communication," *IEEE Communications Surveys & Tutorials*, vol. 24, no. 2, pp. 994–1034, 2022.
- [8] B. K. Chalise and B. Himed, "Performance tradeoff in a unified multi-static passive radar and communication system," in *2018 IEEE Radar Conference (RadarConf18)*, 2018, pp. 0653–0658.
- [9] Z. Wei, H. Qu, Y. Wang, X. Yuan, H. Wu, Y. Du, K. Han, N. Zhang, and Z. Feng, "Integrated Sensing and Communication Signals Toward 5G-A and 6G: A Survey," *IEEE Internet of Things Journal*, vol. 10, no. 13, pp. 11 068–11 092, 2023.
- [10] J. A. Zhang, F. Liu, C. Masouros, R. W. Heath, Z. Feng, L. Zheng, and A. Petropulu, "An Overview of Signal Processing Techniques for Joint Communication and Radar Sensing," *IEEE Journal of Selected Topics in Signal Processing*, vol. 15, no. 6, pp. 1295–1315, 2021.
- [11] D. Ma, N. Shlezinger, T. Huang, Y. Liu, and Y. C. Eldar, "FRAc: FMCW-Based Joint Radar-Communications System Via Index Modulation," *IEEE Journal of Selected Topics in Signal Processing*, vol. 15, no. 6, pp. 1348–1364, 2021.
- [12] J. A. Zhang, X. Huang, Y. J. Guo, J. Yuan, and R. W. Heath, "Multibeam for Joint Communication and Radar Sensing Using Steerable Analog Antenna Arrays," *IEEE Transactions on Vehicular Technology*, vol. 68, no. 1, pp. 671–685, 2019.
- [13] E. Grossi, M. Lops, L. Venturino, and A. Zappone, "Opportunistic Radar in IEEE 802.11ad Networks," *IEEE Transactions on Signal Processing*, vol. 66, no. 9, pp. 2441–2454, 2018.
- [14] Q. Zhang, H. Sun, X. Gao, X. Wang, and Z. Feng, "Time-Division ISAC Enabled Connected Automated Vehicles Cooperation Algorithm Design and Performance Evaluation," *IEEE Journal on Selected Areas in Communications*, vol. 40, no. 7, pp. 2206–2218, 2022.
- [15] K. Ji, Q. Zhang, Z. Wei, Z. Feng, and P. Zhang, "Networking Based ISAC Hardware Testbed and Performance Evaluation," *IEEE Communications Magazine*, vol. 61, no. 5, pp. 76–82, 2023.
- [16] Q. Zhang, K. Ji, Z. Wei, Z. Feng, and P. Zhang, "Joint Communication and Sensing System Performance Evaluation and Testbed: A Communication-Centric Approach," *IEEE Network*, pp. 1–1, 2024.
- [17] Q. Shi, L. Liu, S. Zhang, and S. Cui, "Device-free sensing in OFDM cellular network," *IEEE Journal on Selected Areas in Communications*, vol. 40, no. 6, pp. 1838–1853, 2022.
- [18] W. Mao, Y. Lu, C.-Y. Chi, B. Ai, Z. Zhong, and Z. Ding, "Communication-Sensing Region for Cell-Free Massive MIMO ISAC Systems," *IEEE Transactions on Wireless Communications*, 2024.
- [19] L. Xie, S. Song, and K. B. Letaief, "Networked sensing with AI-empowered interference management: Exploiting macro-diversity and array gain in perceptive mobile networks," *IEEE Journal on Selected Areas in Communications*, 2023.
- [20] X. Chen, Z. Feng, Z. Wei, X. Yuan, P. Zhang, J. A. Zhang, and H. Yang, "Multiple Signal Classification Based Joint Communication and Sensing System," *IEEE Transactions on Wireless Communications*, vol. 22, no. 10, pp. 6504–6517, 2023.
- [21] S. Li, W. Yuan, C. Liu, Z. Wei, J. Yuan, B. Bai, and D. W. K. Ng, "A Novel ISAC Transmission Framework Based on Spatially-Spread Orthogonal Time Frequency Space Modulation," *IEEE Journal on Selected Areas in Communications*, vol. 40, no. 6, pp. 1854–1872, 2022.
- [22] F. Dong, F. Liu, Y. Cui, W. Wang, K. Han, and Z. Wang, "Sensing as a Service in 6G Perceptive Networks: A Unified Framework for ISAC Resource Allocation," *IEEE Transactions on Wireless Communications*, vol. 22, no. 5, pp. 3522–3536, 2023.
- [23] Z. Hu, Z. Bai, Y. Yang, Z. Zheng, K. Bian, and L. Song, "UAV aided aerial-ground IoT for air quality sensing in smart city: Architecture, technologies, and implementation," *IEEE Network*, vol. 33, no. 2, pp. 14–22, 2019.
- [24] V. C. Chen, *The micro-Doppler effect in radar*. Artech house, 2019.
- [25] L. Potter, D.-M. Chiang, R. Carriere, and M. Gerry, "A GTD-based parametric model for radar scattering," *IEEE Transactions on Antennas and Propagation*, vol. 43, no. 10, pp. 1058–1067, 1995.
- [26] Q. Wang, M. Pepin, A. Wright, R. Dunkel, T. Atwood, B. Santhanam, W. Gerstle, A. W. Doerry, and M. M. Hayat, "Reduction of vibration-induced artifacts in synthetic aperture radar imagery," *IEEE Transactions on Geoscience and Remote Sensing*, vol. 52, no. 6, pp. 3063–3073, 2013.
- [27] V. Chen, F. Li, S.-S. Ho, and H. Wechsler, "Micro-Doppler effect in radar: phenomenon, model, and simulation study," *IEEE Transactions on Aerospace and Electronic Systems*, vol. 42, no. 1, pp. 2–21, 2006.
- [28] H. C. A. Costa, S. J. Myint, C. Andrich, S. W. Giehl, C. Schneider, and R. S. Thomä, "Modelling micro-doppler signature of drone propellers in distributed isac," in *2024 IEEE Radar Conference (RadarConf24)*, 2024, pp. 1–6.
- [29] Q. Wang, M. Pepin, A. Wright, R. Dunkel, T. Atwood, B. Santhanam, W. Gerstle, A. W. Doerry, and M. M. Hayat, "Reduction of Vibration-Induced Artifacts in Synthetic Aperture Radar Imagery," *IEEE Transactions on Geoscience and Remote Sensing*, vol. 52, no. 6, pp. 3063–3073, 2014.
- [30] Peng, Silong and Hwang, Wen-Liang, "Null Space Pursuit: An Operator-based Approach to Adaptive Signal Separation," *IEEE Transactions on Signal Processing*, vol. 58, no. 5, pp. 2475–2483, 2010.
- [31] S. Peng and W.-L. Hwang, "Adaptive Signal Decomposition Based on Local Narrow Band Signals," *IEEE Transactions on Signal Processing*, vol. 56, no. 7, pp. 2669–2676, 2008.
- [32] X. Hu, S. Peng, and W.-L. Hwang, "Operator based multicomponent AM-FM signal separation approach," in *2011 IEEE International Workshop on Machine Learning for Signal Processing*, 2011, pp. 1–6.
- [33] G. Yu, M. Yu, and C. Xu, "Synchroextracting Transform," *IEEE Transactions on Industrial Electronics*, vol. 64, no. 10, pp. 8042–8054, 2017.
- [34] 3GPP, "Technical Specification Group Radio Access Network; NR; Physical channels and modulation," 3GPP TR 38.211, September 2021, rel. 16.
- [35] T. Li, B. Wen, Y. Tian, S. Wang, and Y. Yin, "Optimized Radar Waveform Parameter Design for Small Drone Detection Based on Echo Modeling and Experimental Analysis," *IEEE Access*, vol. 7, pp. 101 527–101 538, 2019.
- [36] S. Radkowski and P. Szulim, "Analysis of vibration of rotors in unmanned aircraft," in *2014 19th International Conference on Methods and Models in Automation and Robotics (MMAR)*, 2014, pp. 748–753.
- [37] N. E. Huang, Z. Shen, S. R. Long, M. C. Wu, H. H. Shih, Q. Zheng, N.-C. Yen, C. C. Tung, and H. H. Liu, "The empirical mode decomposition and the Hilbert spectrum for nonlinear and non-stationary time series analysis," *Proceedings of the Royal Society of London. Series A: mathematical, physical and engineering sciences*, vol. 454, no. 1971, pp. 903–995, 1998.
- [38] K. Dragomiretskiy and D. Zosso, "Variational mode decomposition," *IEEE transactions on signal processing*, vol. 62, no. 3, pp. 531–544, 2013.
- [39] D. K. Barton, *Radar equations for modern radar*. Artech House, 2013.
- [40] G. T. 38.104, "NR; Base Station (BS) radio transmission and reception," 2019.
- [41] C. Sturm and W. Wiesbeck, "Waveform Design and Signal Processing Aspects for Fusion of Wireless Communications and Radar Sensing," *Proceedings of the IEEE*, vol. 99, no. 7, pp. 1236–1259, 2011.